Origin of Self-Reversed Thermoremanent Magnetization

Richard J. Harrison,[1] Takeshi Kasama,[2,3] Thomas A. White,[3] Edward T. Simpson,[3] and Rafal E. Dunin-Borkowski[3,2]

[1]*Department of Earth Sciences, University of Cambridge, Downing Street, Cambridge CB2 3EQ, United Kingdom*
[2]*Frontier Research System, The Institute of Physical and Chemical Research, Hatoyama, Saitama 350-0395, Japan*
[3]*Department of Materials Science and Metallurgy, University of Cambridge, Pembroke Street, Cambridge CB2 3QZ, United Kingdom*

(Received 2 September 2005; published 21 December 2005)

The ability of certain magnetic minerals to acquire a remanent magnetization that opposes the direction of the Earth's magnetic field has fascinated rock magnetists since its discovery in 1951. Here, we determine the origin of this phenomenon, which is termed self-reversed thermoremanent magnetization (SR-TRM). We present direct transmission electron microscopy observations of negative exchange coupling across antiphase domain boundaries (APBs) in ilmenite-hematite. This coupling is linked intrinsically to the origin of SR-TRM and is responsible for the formation of two new classes of magnetic domain wall at APBs. We present simulations of the chemical and magnetic structure of the APBs and show that SR-TRM is generated by coupling between strongly ferrimagnetic Ti-rich domains and weakly ferrimagnetic Fe-rich domains, which form during the transition from short- to long-range cation order.

DOI: 10.1103/PhysRevLett.95.268501 PACS numbers: 91.60.Pn, 75.70.Cn, 75.75.+a, 91.25.Ng

In 1951, Néel's prediction that some minerals could become magnetized antiparallel to an applied magnetic field threatened to discredit geological observations suggesting that the Earth's magnetic field had reversed its polarity many times throughout history [1]. Examples of self-reversed thermoremanent magnetization (SR-TRM) were soon discovered in volcanic rocks from Haruna [2] and attributed to intermediate members of the ilmenite-hematite solid solution ($FeTiO_3$-Fe_2O_3) [3]. The mechanism of SR-TRM is still poorly understood, but is thought to require the presence of two phases within the mineral [4]. A weakly magnetic, metastable "x phase" is thought to be the first phase to become magnetized on cooling, acquiring a normal TRM in the presence of an applied field. A strongly magnetic, stable phase then becomes magnetized at a lower temperature. This phase acquires a reversed TRM as a result of negative exchange coupling to the x phase. SR-TRM in ilmenite-hematite occurs in grains that have cooled rapidly through a high-temperature cation ordering phase transition to form nanoscale antiphase domains (APDs). An alternating sequence of Fe-rich and Ti-rich cation layers is established in each APD. The ordering of the layers is interchanged between adjacent domains, which are separated by cation-disordered antiphase boundaries (APBs). Since SR-TRM is observed only when the density of APBs is sufficiently high (i.e., when the APDs are sufficiently small), it has been proposed that Fe-enriched APBs act as the x phase and that negative magnetic exchange coupling between APBs and APDs is the most likely cause of SR-TRM [5–7].

In order to examine the nature of magnetic exchange coupling at APBs in ilmenite-hematite, a solid solution containing 70% ilmenite and 30% hematite (ilm70) was synthesized at 1573 K, quenched through the cation ordering phase transition and annealed for 10 hours at 1023 K. The sample, which contained a microstructure of APDs separated by APBs, was examined using off-axis electron holography, a technique that allows the phase shift of a high-energy electron wave to be recorded in a transmission electron microscope (TEM) [8,9]. The phase shift is used to provide a quantitative, noninvasive measurement of the magnitude and direction of the magnetic flux in the material with nanometer spatial resolution. Prior to each measurement, the sample was saturated magnetically by tilting it to an angle of $+30°$ to the horizontal and exposing it to the 2 T vertical field of the objective lens of the Philips CM300ST TEM. It was then tilted to $-30°$ and exposed to a chosen field, which was then removed. All holograms were recorded digitally at 300 kV, with the objective lens switched off and the sample at zero tilt. Representative results are shown in Figs. 1(a)–1(c). Each figure, which is derived from the gradient of the measured phase shift, shows a magnetic remanent state obtained at a different stage of the switching process. The direction and magnitude of the in-plane magnetic flux are defined by the hue and intensity of the color, respectively.

The magnetization in this sample is constrained by shape and magnetocrystalline anisotropy to lie parallel or antiparallel to the intersection of the specimen plane with the (001) crystallographic plane (indicated by the double black arrow in Fig. 1). As a result, regions with strong in-plane magnetization appear either blue or green. Regions that have weak in-plane magnetization appear as dark bands. Analysis (see Fig. 2) shows that the dark bands in Fig. 1 are associated with three distinct types of magnetic wall. A fingerlike region of reversed magnetization [labeled "1" in Fig. 1(a)] enlarges by the movement of its left-hand boundary as the applied field is increased [Fig. 1(b)]. This left-hand boundary is a conventional free-standing 180° Bloch wall. In contrast, in regions where a 180° reversal in magnetization coincides exactly with the position of an APB (e.g., at regions labeled "2"), the reversal results from negative exchange coupling, and occurs without any out-of-plane rotation of the magnetic

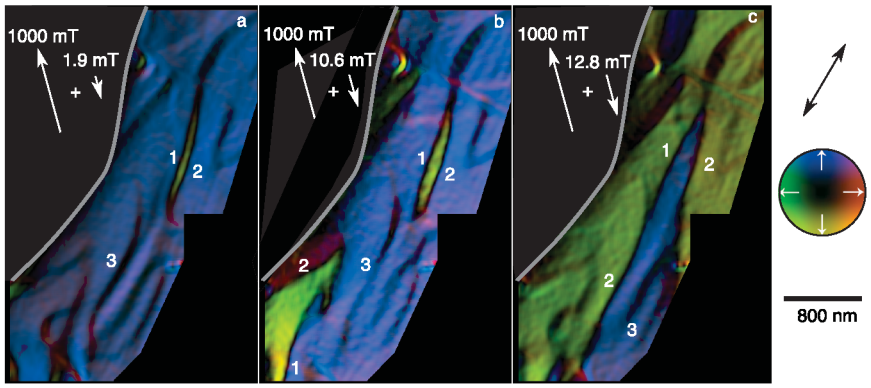

FIG. 1 (color). Magnetic microstructure of ilm70 containing several APDs. The sample edge is indicated by the gray line. Prior to each measurement, the sample was exposed to a saturating field with an in-plane/out-of-plane component of $+1000/+1732$ mT, followed by a smaller field with an in-plane/out-of-plane component of (a) $-1.9/+3.3$ mT, (b) $-10.6/+18.4$ mT, (c) $-12.8/+22.2$ mT. White arrows indicate the direction of the in-plane component of the applied field. The hue and intensity of the color indicates the direction and magnitude of the in-plane component of the magnetic flux in the sample in field-free conditions, as defined by the color wheel on the right. The blue-purple and green-yellow colors correspond to equal and opposite in-plane magnetizations in the direction indicated by the black double arrow. The dark bands indicate regions with weak in-plane magnetization (magnetic domain walls). Dark bands that separate regions of blue and green color correspond to 180° magnetic and chemical walls (e.g., at regions labeled "1" and "2," respectively). Dark bands that are surrounded by regions of the same color correspond to 0° magnetic walls (e.g., at regions labeled "3").

moments. We refer to this type of boundary as a 180° "chemical" wall. A third type of magnetic wall appears as thick black bands, which are coincident with the positions of APBs (e.g., at regions labeled "3"). Such walls form when the negative exchange coupling between adjacent APDs is overcome at sufficiently large fields. We refer to these walls as 0° magnetic walls.

In the absence of demagnetizing fields outside the sample, the measured phase shift, ϕ, varies with distance x according to the equation:

$$\phi(x) = -\frac{e}{\hbar}\int B(x)t(x)dx, \tag{1}$$

where B is the in-plane component of magnetic induction in the sample (in a direction perpendicular to x) and t is the sample thickness. Equation (1) provides the basis for the experimental measurement of magnetic induction. The out-of-plane rotation of moments at a 180° Bloch wall is generally described by an expression of the form [10]

$$B(x) = B_0 \tanh\left(\frac{x}{w}\right), \tag{2}$$

where B_0 is the saturation induction and $2w$ is the wall width. Equation (2) provides an excellent fit to the phase profile of a 180° Bloch wall for $2w = 19$ nm [Fig. 2(a)]. In contrast, the phase profile on either side of a 180° chemical wall is nonlinear (see below), and the reversal in the slope of the phase at the center of the wall occurs much more abruptly [Fig. 2(b)]. A fit to the central portion of the wall yields $2w = 7$ nm [dashed line in Fig. 2(b)]. This value is close to the resolution limit of the measurements and provides an upper limit for the width of the chemical wall. For a 0° wall, the phase shift is described excellently by a profile of the form

$$B(x) = B_0 \tanh^2\left(\frac{x}{w}\right). \tag{3}$$

The $\tanh^2$ form results from the superposition of a 180° Bloch wall and a 180° chemical wall. An average of 13 measurements yielded $2w = (50 \pm 14)$ nm for 0° walls. Previous studies demonstrated that SR-TRM was observed only when APDs were below 80–100 nm in size. We suggest that this limit is imposed by the formation of 0° walls, which allow negative exchange coupling between adjacent domains to be overcome when the APDs are larger than approximately 50 nm in size.

A computational model of coupled cation and magnetic ordering was used to interpret the experimental measurements and, in particular, the nature of exchange coupling at APBs [11]. Spins are constrained to lie in the plane, so shape anisotropy and magnetostriction can be neglected. The starting point for the simulations was an $8 \times 8 \times 8$ supercell of fully cation-ordered ilm70, comprising 48 alternating Fe-rich and Ti-rich cation layers. APBs were introduced by interchanging Fe^{2+} and Ti^{4+} cations in half of the supercell. Monte Carlo simulations were performed at 850 and 1100 K (below the cation ordering transition temperature) to "anneal" the system, allowing it to relax to a state of metastable cation order. After annealing, the cation configuration was frozen in, and simulations of magnetic ordering were performed at lower temperatures.

The degree of cation order is defined as [12]

$$Q = \frac{N_{\mathrm{Ti}}^{B} - N_{\mathrm{Ti}}^{A}}{N_{\mathrm{Ti}}^{A} + N_{\mathrm{Ti}}^{B}}, \tag{4}$$

where N_{Ti}^{A} and N_{Ti}^{B} are the number of Ti cations on adjacent cation layers (labeled A and B, respectively). Annealing at 850 K generated a mixture of ordered ($Q = 1$) and anti-

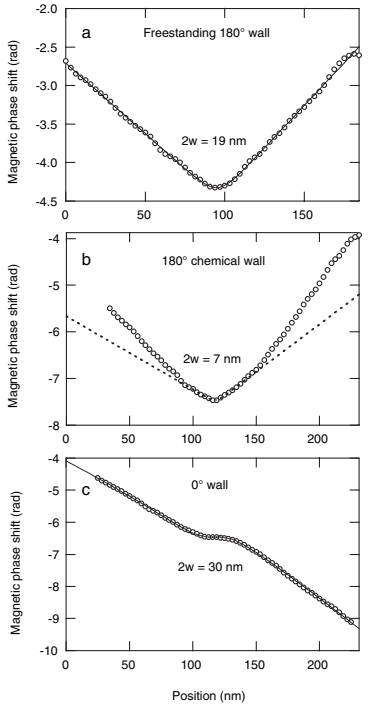

FIG. 2. Profiles of the holographic phase shift, ϕ, across three distinct types of magnetic domain wall. The gradient of each profile is proportional to the in-plane component of the magnetic flux [Eq. (1)]. (a) A freestanding 180° Bloch wall. The solid line is a least-squares fit to the observed profile, obtained by using Eqs. (1) and (2) and yielding a wall width of 19 nm. (b) A 180° chemical wall that is coincident with an APB. The dashed line is a fit to the central portion of the wall, obtained by using Eqs. (1) and (2) and yielding a wall width of 7 nm. (c) A 0° magnetic wall that is coincident with the same APB as in (b). The slope of the phase profile has the same sign on either side of the wall, indicating that the direction of magnetization is the same. The solid line is a fit to the profile, obtained using Eqs. (1) and (3) and yielding a wall width of 30 nm.

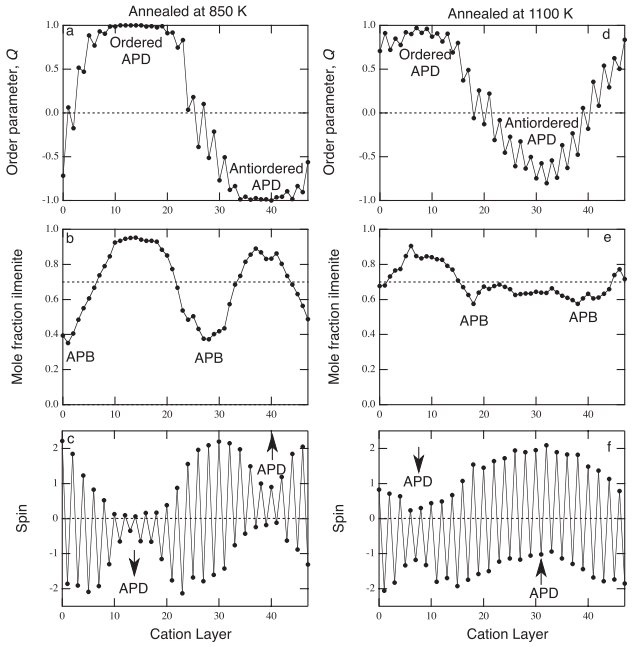

FIG. 3. Simulated cation and magnetic structure of APBs. Plots show the average values of the order parameter, Q, the mole fraction of ilmenite, and the spin on each of the 48 layers of an $8 \times 8 \times 8$ supercell for ilm70 annealed at (a)–(c) 850 K and (d)–(f) 1100 K. (a) The order parameter profile for a system with short-range cation order shows fully ordered and antiordered APDs ($Q = 1$ and $Q = -1$, respectively) separated by disordered APBs ($Q = 0$). (b) The composition profile indicates that the APBs are enriched in hematite relative to the bulk composition (dashed line). (c) The magnetic structure obtained at 25 K consists of an alternating sequence of up (+ve) and down (−ve) spins throughout the supercell. The magnitude of the spins is modulated by the local composition and the degree of cation order. The APD centered on layer 14 is ferrimagnetic with a net negative spin; the APD centered on layer 40 is ferrimagnetic with a net positive spin (indicated by the arrows). (d) The order parameter profile for a system with partial long-range order shows a fully ordered APD ($Q \sim 1$) and a less well (anti)ordered APD ($Q \sim -0.75$). (e) The composition profile shows that the well-ordered APD has >70% ilmenite, whereas the less-well-ordered APD has <70% ilmenite. Evidence for Fe enrichment at the APBs is also seen. (f) The spin profile at 25 K shows that the well-ordered APD is strongly ferrimagnetic, whereas the ferrimagnetic spin of the less-well-ordered APD is decreased by the influence of the boundary regions.

ordered ($Q = -1$) APDs that were separated by cation-disordered APBs [$Q = 0$, Fig. 3(a)]. This state corresponds to high short-range cation order ($\langle Q \rangle = 0$, $\langle Q^2 \rangle > 0$) [13]. The APBs are enriched in Fe relative to the APDs [a fundamental assumption in all models of SR-TRM, Fig. 3(b)], with the magnitude of this enrichment enhanced by the immisciblity of ilmenite and hematite at this temperature. Negative exchange coupling between adjacent cation layers leads to an alternating sequence of up and down spins throughout the supercell [Fig. 3(c)]. The center of the APB is antiferromagnetic, due to an equal concentration of Fe on adjacent layers. The ordered APD is ferrimagnetic, due to an unequal concentration of Fe on adjacent layers. The adjacent antiordered APD is also ferrimagnetic, but the net moment is antiparallel to that in the ordered APD. This reversal in the net moment results in the appearance of 180° chemical walls in Fig. 1. Unlike for a conventional 180° Bloch wall, no out-of-plane rotation of magnetic moments takes place. As the net magnetization at any point in the wall is proportional to Q [14], the nonlinearity of the phase profile in Fig. 2(b) is a quantitative measure of the variation in Q across the APB, and suggests that Q continues to vary well away from the center of the wall.

Annealing at 1100 K results in partial disorder in the antiordered domain, as the system attempts to transform from short-range ($\langle Q \rangle = 0$) to long-range ($\langle Q \rangle > 0$) cation order, driven by the energy released by removing the APBs [Fig. 3(d)]. Although ilmenite and hematite are miscible at 1100 K, some compositional heterogeneity remains [Fig. 3(e)]. There is evidence of slight Fe enrichment at the APBs and, more significantly, partitioning of Fe be-

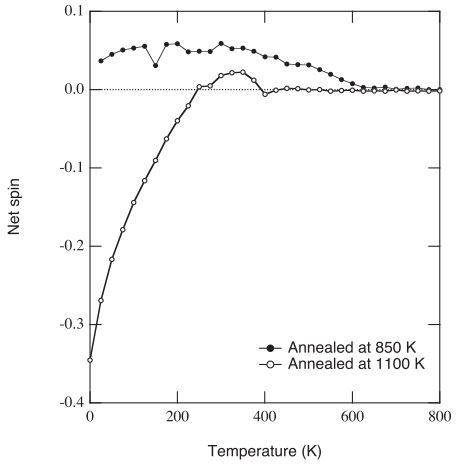

FIG. 4. Net ferrimagnetic spin, simulated as a function of temperature for systems with short-range cation order (supercell annealed at 850 K, closed circles) and partial long-range cation order (supercell annealed at 1100 K, open circles). The system with partial long-range order displays a self-reversal of net ferrimagnetic spin at ~250 K.

tween the domains. The well-ordered domain contains >70% ilmenite, whereas the less well (anti)ordered domain contains <70% ilmenite. The spin profile [Fig. 3(f)] indicates a strong ferrimagnetic moment associated with the ordered domain and a weak ferrimagnetic moment with the antiordered domain and boundary regions.

The Fe-enriched antiordered regions fulfill all of the requirements of the *x* phase: they are the first to become magnetically ordered on cooling; they are very close to being antiferromagnetic, but carry a small net moment due to partial cation order; they are negatively exchanged coupled to the neighboring ordered APDs [Fig. 3(f)]; they are metastable, appearing only in systems that are partway through the transformation from short- to long-range order. These properties lead to a self-reversal in net magnetization on cooling (Fig. 4). Magnetic ordering in the Fe-enriched antiordered domain sets in below 425 K, yielding a weak positive ferrimagnetic moment. Magnetic order spreads to the ordered domain on cooling below 350 K. Below 250 K, the moment of the antiordered domain is outweighed by the oppositely oriented moment of the ordered domain, and the net magnetization reverses. In contrast, no net reversal is observed in the 850 K simulation, which contains equally well-ordered and antiordered domains, despite the enhanced enrichment of Fe at the APB.

The experimental observations and computational simulations of exchange coupling at APBs provide an explanation for the origin of SR-TRM in natural dacitic pumices. In a separate study, microscopic studies of ilmenite-hematite grains from the Nevado del Ruiz and Pinatubo volcanoes revealed the presence of compositional and magnetic zoning, with the rims of the grains being slightly richer in Fe than the cores [15]. The rims are cation-disordered and antiferromagnetic, while the cores are cation-ordered and ferrimagnetic, leading to the suggestion that the rims act as the *x* phase. A transition from short- to long-range cation order will occur between the rim and the core. We suggest that this region of partial long-range order, and not the Fe-enriched rim, acts as the source of SR-TRM. This conclusion is supported by TEM observations of samples from Mount Pinatubo, which reveal the presence of ordered APDs with a size of 20–40 nm that are embedded in a relatively disordered matrix in the interior of the grains. This microstructure is consistent with the present predicted mixture of well-ordered and less well (anti)ordered domains in a transitional state between short-range and long-range cation order [Fig. 3(d)] [16]. The ordered APDs are below the 50 nm limit required to prevent the formation of 0° walls, and will therefore be negatively exchange coupled to the surrounding matrix, resulting in SR-TRM according to the mechanism introduced here.

This research was supported by grants from the Research Council of Norway (Grant No. 163556 "The nature and origin of natural magnetic nanoscale materials" to S. M.) and by support from NERC (NE/B501339/1 "Mineral magnetism at the nanometre scale" to R. J. H.). R. D. B. thanks the Royal Society for support.

[1] L. Néel, Ann. Geophys. **7**, 90 (1951).
[2] T. Nagata, S. Akimoto, and S. Uyeda, Proc. Jpn. Acad. **27**, 643 (1951).
[3] Y. Ishikawa and S. Akimoto, J. Phys. Soc. Jpn. **12**, 1083 (1957).
[4] Y. Ishikawa and Y. Syono, J. Phys. Chem. Solids **24**, 517 (1963).
[5] G. L. Nord and C. A. Lawson, Am. Mineral. **74**, 160 (1989).
[6] G. L. Nord and C. A. Lawson, J. Geophys. Res. **97**, 10 897 (1992).
[7] K. A. Hoffman, J. Geophys. Res. **97**, 10 883 (1992).
[8] R. E. Dunin-Borkowski, M. R. McCartney, and D. J. Smith, in *Encyclopedia of Nanoscience and Nanotechnology*, edited by H. S. Nalwa (American Scientific Publishers, Stevenson Ranch, CA, 2004), Vol. 3, pp. 41–99.
[9] R. J. Harrison, R. E. Dunin-Borkowski, and A. Putnis, Proc. Natl. Acad. Sci. U.S.A. **99**, 16 556 (2002).
[10] L. D. Landau and E. M. Lifshitz, *Statistical Physics* (Pergamon Press, Oxford, 1980).
[11] P. Robinson, R. J. Harrison, S. A. McEnroe, and R. B. Hargraves, Nature (London) **418**, 517 (2002).
[12] R. J. Harrison, U. Becker, and S. A. T. Redfern, Am. Mineral. **85**, 1694 (2000).
[13] R. J. Harrison and S. A. T. Redfern, Phys. Chem. Miner. **28**, 399 (2001).
[14] N. E. Brown, A. Navrotsky, G. L. Nord, and S. K. Banerjee, Am. Mineral. **78**, 941 (1993).
[15] V. Hoffmann and K. T. Fehr, Geophys. Res. Lett. **23**, 2835 (1996).
[16] M. Prévot, K. A. Hoffman, A. Goguitchaichvili, J.-C. Doukhan, V. Schcherbakov, and M. Bina, Phys. Earth Planet. Inter. **126**, 75 (2001).